Japanese Journal of Applied Physics

REGULAR PAPER

Electrical properties and conduction mechanisms of heavily B^+-ion-implanted type IIa diamond: effects of temperatures during the ion implantation and postannealing upon electrical conduction

Japanese Journal of Applied Physics **59**, 021003 (2020) **REGULAR PAPER**
https://doi.org/10.35848/1347-4065/ab699c

Electrical properties and conduction mechanisms of heavily B^+-ion-implanted type IIa diamond: effects of temperatures during the ion implantation and postannealing upon electrical conduction

Yuhei Seki, Yasushi Hoshino*, and Jyoji Nakata

Department of Mathematics and Physics, Kanagawa University, 2946, Tsuchiya, Hiratsuka, Kanagawa 259-1293, Japan

*E-mail: yhoshino@kanagawa-u.ac.jp

Received December 13, 2019; accepted January 9, 2020; published online February 7, 2020

We investigated the electrical properties and conduction mechanism of heavily B^+-implanted type IIa diamond with respect to the implantation and postannealing temperatures. The B atoms were shallowly implanted with a flat concentration of 3.5×10^{19} cm^{-3} at RT and 900 °C; these samples were finally annealed at 1150 °C, 1300 °C and 1450 °C. We consequently confirmed *p*-type conductivity and typical ionization energy of acceptor B in a wide measured temperature range. The doping efficiency progressed remarkably well and attained 78% and the Hall mobility at RT was realized to be 108 cm^{2}V^{-1}s^{-1} for the RT-implanted sample followed by annealing at 1300 °C. On the other hand, hot B^+ implantation at 900 °C slightly degraded the electrical properties. The higher-temperature annealing at 1450 °C after B^+ ion implantation promoted hopping conduction fairly well at a lower measured temperature range below around RT. We systematically investigated the hopping conduction mechanism based on theoretical relations. © 2020 The Japan Society of Applied Physics

1. Introduction

Effective impurity doping into single-crystalline diamond substrates has been a crucial subject in the application of high-power and high-frequency electronic devices.[1–3] Impurity doping has usually been performed in the synthesis process of diamond film by chemical vapor deposition (CVD).[4–7] It is well known that impurity doping by ion implantation is quite superior to that in epitaxial growth in terms of the merits of short process time, large doping area and low financial cost. In addition, one can easily introduce any dopants in the desired area and depth with an accurate concentration; therefore, it is a common tool for fabricating Si- and GaAs-based semiconductor devices. In the case of diamond semiconductor fabrication, impurity doping by ion implantation has not been practically accomplished, in spite of research in this regard for several decades.[8–18]

According to previous studies, the substrate quality and temperatures during ion implantation and postannealing are regarded as significantly important parameters for the final electronic properties of diamond semiconductor. Concerning the substrate temperature during B^+ ion implantation for the formation of *p*-type semiconductor, various temperatures from −196 °C to 400 °C have been investigated so far. Prins performed impurity doping by ion implantation at −196 °C followed by rapid thermal annealing.[8–11] Uzan-Saguy et al. and Fontaine et al. then developed the doping process and obtained a small doping efficiency of 2% at most.[12,14] In the case of RT implantation, Vogel et al. carried out B δ-doping by 2 MeV B^+ ion implantation followed by annealing at higher than 1500 °C. The doping efficiency was slightly improved to 30% for the sample with a fluence of 10^{14} cm^{-2}. Tsubouchi et al. recently performed B^+ ion implantation with B concentrations of 10^{18}–10^{21} cm^{-3} at 400 °C followed by 1450 °C and 1600 °C annealing. In the heavily B^+-implanted sample with 5×10^{19} cm^{-3}, the doping efficiency was only 9%.

In the aspect of application to high-power and high-frequency devices, the establishment of the fabrication process of low-resistance layer with highly controlled *p*- and *n*-type conductivity using ion implantation is the inevitable issue. In the previous letter, we reported the progress of the electrical properties for type IIa diamond substrates doped by B^+ ion implantation at RT followed by relatively low-temperature annealing at 1150 °C and 1300 °C.[19] In the present study, we have further investigated the dependence of electrical properties of B^+-implanted type IIa diamond substrates on the implantation temperatures and postannealing temperatures. Finally, we have comprehensively clarified the mechanisms of hopping conduction, especially those appearing in the high-temperature postannealing samples, based on the theoretical relations. We also qualitatively referred to the reasons such excellent electrical properties can be obtained.

2. Experimental

Type IIa diamond substrates of standard grade with a typical size of 3×3 mm^2 synthesized by the CVD method were purchased from Element Six Ltd. These samples were mechanically polished in advance at Syntek Co. Ltd. The average surface roughness was evaluated by atomic force microscope to be less than 0.03 nm. The atomically flat samples were then treated with a typical wet chemical cleaning process for diamond: dipping in H_2SO_4 and HNO_3 solution followed by diluted NH_3 and H_2O_2 solution. The samples were immediately introduced into a vacuum chamber for B^+ ion implantation, whose base pressure was achieved below 10^{-5} Pa. The accelerated $^{11}B^+$ ions with eight different energies from 5–60 keV were implanted into the substrates to obtain a flat concentration from the surface to the ∼130 nm depth. The B^+ ions were implanted at the substrate temperatures of 900 °C or RT to investigate the dependence of doping efficiency on the temperatures during the implantation. The total fluence of B^+ ion was 4.6×10^{14} cm^{-2}, and the fluence for each energy was estimated by TRIM simulation in advance.[20] The concentration and thickness at the plateau region were estimated by secondary ion mass spectroscopy (SIMS) after all electrical properties were measured. Samples were then covered with a thin SiO_2 cap layer ∼100 nm thick by RF sputtering to prevent the surface graphitization during the subsequent high-temperature annealing. We finally annealed the samples

Table I. Electrical properties obtained by Hall effect measurements.

Temperature (implant.)	Temperature (postanneal)	N_B (cm^{-3})	N_A (cm^{-3})	N_D (cm^{-3})	K (%) (N_D/N_A)	D_{eff} (%) (N_A/N_B)	μ_{max} (cm^2/Vs)	E_A (eV)
	1150 °C	3.6×10^{19}	2.8×10^{19}	4.7×10^{18}	18.5	78	90	0.335
RT	1300 °C	3.3×10^{19}	1.7×10^{19}	2.9×10^{18}	19.5	52	108	0.302
	1450 °C	—	—	—	~17.0	—	39	~0.25
	1150 °C	—	$>1.0 \times 10^{19}$	4.8×10^{18}	47.0	—	71	0.375
900 °C	1300 °C	3.5×10^{19}	1.3×10^{19}	4.2×10^{18}	36.5	37	61	0.305
	1450 °C	—	—	—	~20.0	—	19	~0.21

in a quartz furnace in Ar ambient. After the annealing, the deposited SiO_2 layer was completely removed by wet HF treatment and the electrical properties were then measured. We adopted the postannealing temperatures of 1150 °C, 1300 °C and 1450 °C, and carried out the electrical measurements for the samples postannealed at each temperature. The preparation processes are briefly listed in Table I.

The electrical measurements of resistivity and Hall effect based on the van der Pauw method were carried out by Resitest 8300 Hall effect apparatus from Toyo Corp. Ohmic electrodes consisting of Au/Pt/Ti multilayers with a diameter of 0.5 mm were then formed near the four corners of the substrates by magnetron sputtering at a substrate temperature of 550 °C followed by 800 °C annealing in high vacuum. The electrical properties of specific resistance, carrier concentration and Hall mobility were measured at sample temperatures from 77–1073 K, though reliable experimental data were obtained above 173 K due to a lack of sufficient electrical activation at such low temperatures.

3. Results and discussion

3.1. Electrical properties in the band conduction region

Figure 1 shows the concentration profile of ^{11}B atoms implanted in type IIa diamond substrates at 900 °C or RT followed by thermal annealing measured with SIMS. The relative sensitivity of secondary ion intensity was calibrated by a well-quantified B-doped diamond in advance. The sputtering rate was determined by the crater depth after SIMS measurement. Black, red, and green curves indicate the depth profile for the samples as implanted at RT and then postannealed at 1150 °C and 1300 °C, respectively. The blue curve shows the depth profile for the 900 °C-implanted sample followed by 1300 °C annealing. The depth profile for the as-implanted sample was fairly broad near the tail edge of the doped layer. This fact is probably attributed to the ion channeling effect during the B^+ implantation because the implantation was performed with low energies from 5–60 keV along almost the normal axis to the substrate surface. After the annealing at high temperatures, the interface became abrupt and a flat B concentration of $\sim 3.5 \times 10^{19}\,cm^{-3}$ was observed from the surface to ~130 nm depth. The thickness of the doped layer was determined from the full width at half-maximum concentration. The concentrations of intrinsically incorporated N and H atoms were estimated to be less than 2×10^{16} and $2 \times 10^{17}\,cm^{-3}$, respectively, by the same SIMS measurement.

Figure 2 shows the carrier concentration (a) and Hall mobility (b) as a function of reciprocal and absolute temperatures, respectively, obtained by Hall effect measurement for the 900 °C-implanted samples followed by 1150 °C, 1300 °C and 1450 °C annealing. The circles denote the results obtained by Hall effect measurement: closed circles indicate the points appearing in *p*-type conduction and open circles are undeterminable points of carrier type. The solid lines indicate the theoretically calculated carrier concentration shown below. It is well known that the temperature-dependent hole concentration (p) can be theoretically formalized by the charge neutrality condition and Fermi–Dirac distribution function, and thus given by the following relation with three parameters of N_A, N_D and E_A:

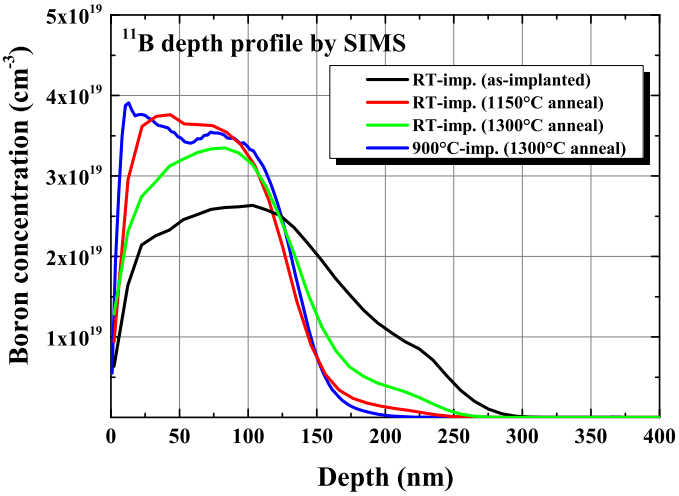

Fig. 1. (Color online) Depth profile of implanted ^{11}B at 900 °C and RT followed by thermal annealing measured by SIMS. Black, red, and green curves indicate the obtained depth profile of ^{11}B for the as-implanted sample at RT, and postannealed samples at 1150 °C and 1300 °C, respectively. Blue curve shows the profile for the 900 °C-implanted sample followed by 1300 °C annealing.

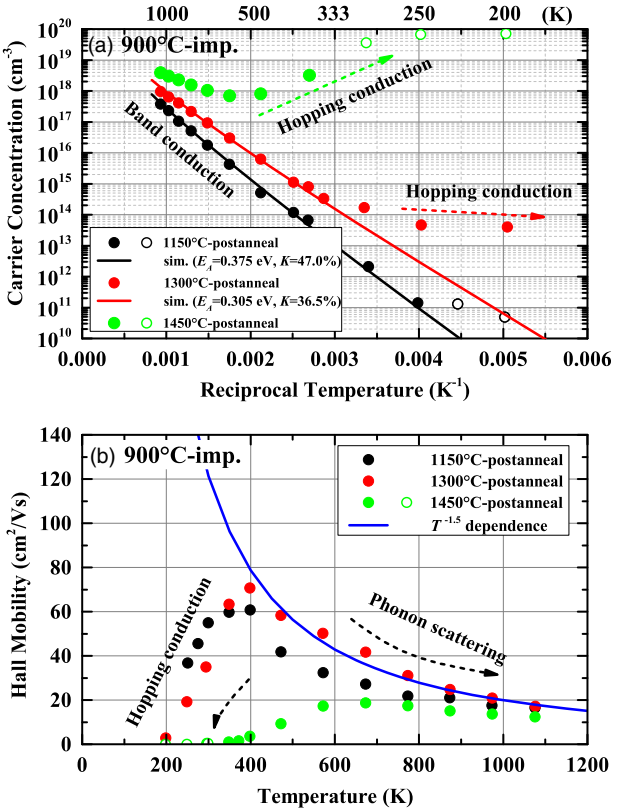

Fig. 2. (Color online) Carrier concentration (a) and Hall mobility (b) as a function of temperature obtained by Hall effect measurement for the 900 °C-implanted samples followed by annealing at 1150 °C (black), 1300 °C (red) and 1450 °C (green). Closed circles show the points appearing in p-type conductivity and open circles are undeterminable points of conduction type.

$$\frac{p(p+N_D)}{N_A-N_D-p}=\frac{2}{g(T)}\left(\frac{2\pi m^* k_B T}{h^2}\right)^{3/2}\exp\left(-\frac{E_A}{k_B T}\right). \quad (1)$$

Here, N_A and N_D are acceptor and donor concentration, respectively; E_A is the activation energy of the acceptor. $g(T)$ and m^* are, respectively, the degeneracy factor and effective hole mass, while these values varied relatively among previous reports. Collins et al. and Fontaine proposed the relations of degeneracy factor; monotonically varying from 4 at low temperatures to 6 at high temperatures.[21,22] We thus adopted the temperature-dependent degeneracy factor $g(T)$ suggested by Collins et al. as follows:

$$g(T)=4+2\exp\left(-\frac{\Delta}{k_B T}\right). \quad (2)$$

Here, Δ is a spin–orbit coupling of diamond with a small split width of $\Delta=6$ meV. Concerning the effective hole mass of diamond, it is relatively scattered around unity, and is not precisely defined. In the previous reports on the analysis of electrical properties, the effective hole mass from 0.7–1.0 was usually used. We then adopted the most commonly referred value of $0.8m_0$ in the present analysis.[12,14,16]

In accordance with Eq. (1), it is found that the carrier concentration does not depend on N_A at enough low-temperature region, except for the hopping region. Hole concentration at such temperatures can be therefore approximated to be a famous relation of,

$$p(K,E_A)=\frac{N_V}{g(T)}\left(\frac{1}{K}-1\right)\exp\left(-\frac{E_A}{k_B T}\right). \quad (3)$$

Here, N_V is the effective density of states. The parameters of activation energy (E_A) and compensation ratio ($K=N_D/N_A$) are directly related to the gradient and offset in the semi-log plot, respectively, indicating that three fitting parameters can be reduced to two parameters of E_A and K. We first best-fitted the hole concentration by assuming K, and E_A at the intermediate temperature region from 300–700 K.

It can be clearly seen in Fig. 2(a) that the carrier concentrations for the 900 °C-implanted samples followed by 1150 °C or 1300 °C annealing were exponentially increased as a function of reciprocal temperature, except for lower temperatures than RT. For the 1450 °C-annealed sample, hopping conduction was dominated below 573 K. We cannot quantitatively discuss the details of temperature-dependent carrier concentrations for the 1450 °C-postannealed sample due to the high contribution of hopping conduction; therefore, we here focus on the properties of the 1150 °C- and 1300 °C-postannealed samples. The details with regard to hopping conduction will be discussed later.

In accordance with Eq. (3), the compensation ratio of the 1150 °C, 1300 °C and 1450 °C-postannealed samples were determined to be 47.0%, 36.5% and 20.0%, respectively, though these were relatively high ratio. The activation energies for the 1150 °C- and 1300 °C-annealed samples were estimated to be 0.375 and 0.305 eV, respectively. The estimated activation energies almost correspond to the acceptor level of substitutional B atom in diamond. The p-type conductivity was confirmed from 250–1073 K for the 1150 °C-postannealed sample, and was entirely observed at temperatures from 173–1073 K after the 1300 °C annealing. It is found that the temperature dependence of hole concentration was significantly decreased below RT, and the tendency was more remarkable in the 1300 °C-postannealed sample. It is suggested that the electrical conduction was dominated by the hopping process in place of band conduction, which will be discussed later in accordance with the temperature-dependent specific resistance.

As can be seen in Fig. 2(b), the Hall mobility took the maximum value of 61 and 71 cm^{2}V^{-1}s^{-1} around RT for the 1150 °C- and 1300 °C-postannealed samples, respectively. The Hall mobility followed the typical temperature dependence of $T^{-3/2}$ at a comparatively higher temperature region than RT. It is indicated that the carrier scattering mechanism is governed by acoustic phonons above RT. The significant decrement of Hall mobility at low temperatures is probably due to the change of conduction mechanism from band conduction to hopping process.

Figure 3 shows the carrier concentration (a) and Hall mobility (b) for the samples B-implanted at RT followed by annealing at 1150 °C, 1300 °C and 1450 °C. The compensation ratio was significantly decreased to less than 20.0% for the 1150 °C (black), 1300 °C (red) and 1450 °C (green) postannealed samples compared to the 900 °C-implanted samples followed by annealing at the same temperatures. By best-fitting the observed hole concentration using Eq. (3), the ionization energy for the 1150 °C-postannealed sample was estimated to be 0.335 eV, and was slightly decreased to

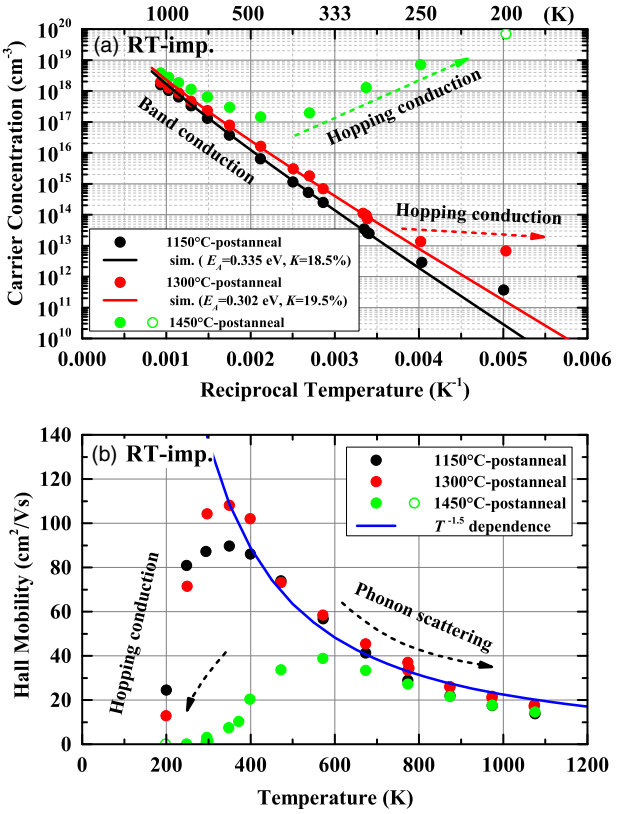

Fig. 3. (Color online) Carrier concentration (a) and Hall mobility (b) as a function of temperature obtained by Hall effect measurement for the RT-implanted samples followed by annealing at 1150 °C (black), 1300 °C (red) and 1450 °C (green). Closed circles show the points appearing in *p*-type conductivity and open circles are undeterminable points of conduction type.

0.302 eV after 1300 °C annealing. The carrier type entirely showed *p*-type conductivity for both samples at the reliable temperature region from 173–1073 K. The Hall mobility depicted in Fig. 3(b) shows the typical relation of $T^{-3/2}$ above RT and took the maximum of 108 cm^2 V^{-1} s^{-1} at RT for the 1300 °C-postannealed sample. Figure 4 shows the previously reported Hall mobilities of diamond B-doped in the CVD process and our present value as a function of acceptor B concentration. It can be found in Fig. 4 that the Hall mobility observed in this study is comparable to the best value expected in the B-doped diamond with the same B concentration.[23–30] The compensation ratio of less than 20.0% was independent of the postannealing temperature for the RT-implanted samples, though the ratio was significantly smaller than that for the 900 °C-implanted sample, as shown in Fig. 2. This fact presumably shows that the higher-temperature implantation is likely to enhance the diffusion and prevent the recombination of generated Frenkel pairs during hot ion implantation, and residual defects are probably developed to irreducible secondary defects. Consequently, we strongly suggest that B-ion implantation as a doping method should be performed at low temperatures such as RT rather than higher temperatures. After determining the parameters of K and E_A, we performed the curve fitting of carrier concentration at higher temperature region (>700 K) by using Eq. (1); eventually determining N_A value, independently.

Figures 5 and 6 show the obtained carrier concentrations as a function of reciprocal temperature calculated by Eq. (1) for the 900 °C- and RT-implanted samples, respectively. The theoretical values depicted by solid curves were calculated by assuming various N_A. Here, K and E_A are the adopted values just determined in the above analysis shown in Figs. 2(a) and 3(a). We can thus uniquely determine the acceptor concentration from the temperature dependence of the hole concentration by iteratively fitting the theoretically calculated values. In the case of the 900 °C-implanted sample followed by 1150 °C annealing, as shown in Fig. 5(a), the carrier

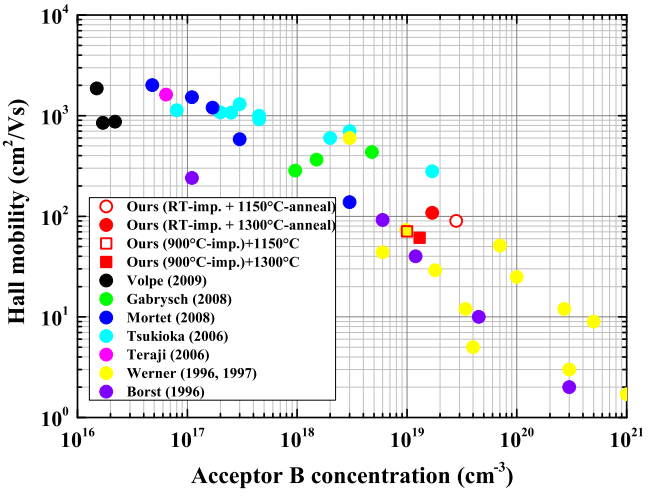

Fig. 4. (Color online) Hall mobilities around RT as a function of acceptor B concentration for previously reported B-doped diamonds by the CVD process as well as our present ones doped by ion implantation at RT and 900 °C.

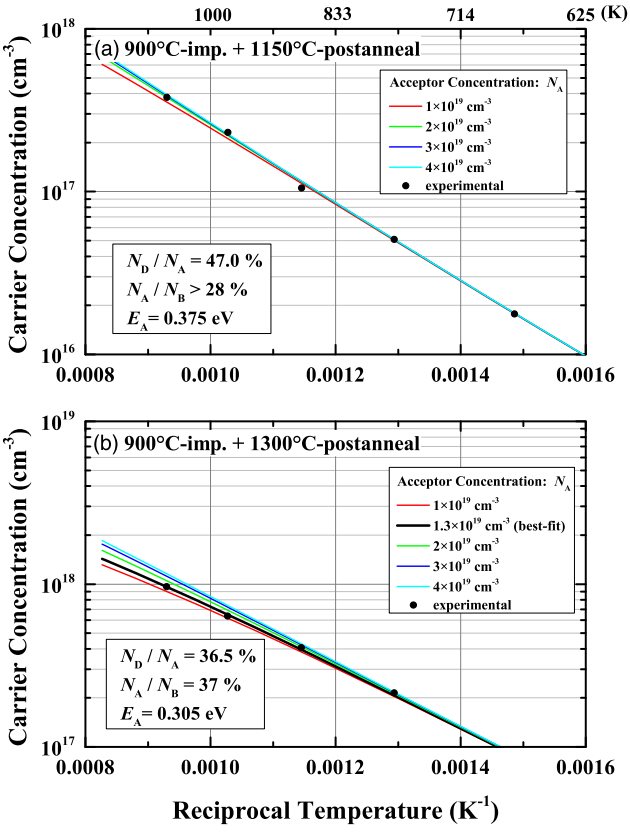

Fig. 5. (Color online) Experimental and simulated carrier concentrations as a function of reciprocal temperature for the 900 °C-implanted samples followed by subsequent annealing at 1150 °C (a) and 1300 °C (b). Solid curves indicate the theoretical values calculated by assuming various N_A.

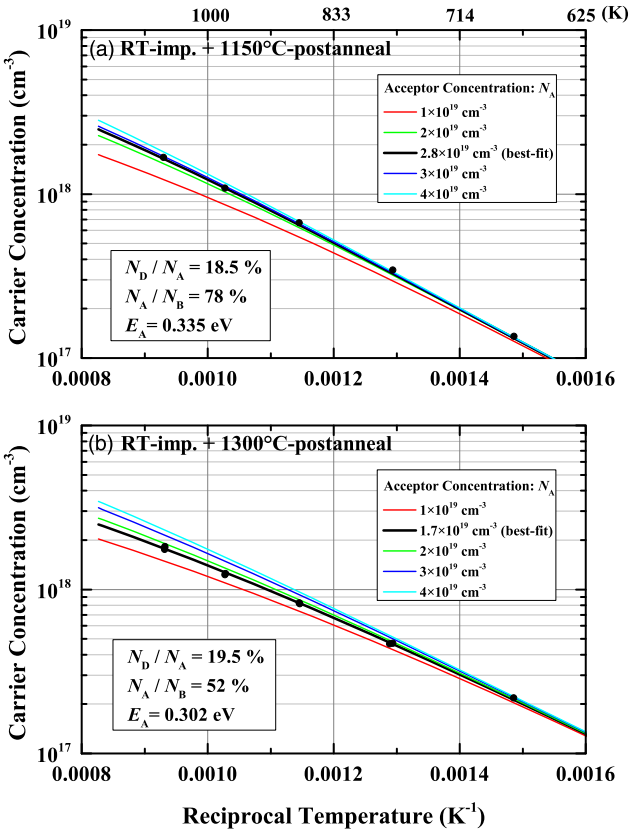

Fig. 6. (Color online) Experimental and simulated carrier concentrations as a function of reciprocal temperature for the RT-implanted samples followed by subsequent annealing at 1150 °C (a) and 1300 °C (b). Solid curves indicate the theoretical values calculated by assuming various N_A.

concentration did not significantly depend on N_A due to high compensation ratio of 50%. We could not therefore precisely determine the adequate N_A value from these data. For the 1300 °C-postannealed sample [Fig. 5(b)], the acceptor concentration was estimated to be $\sim 1.3 \times 10^{19}\,\mathrm{cm}^{-3}$. The doping efficiency ($D_{\mathrm{eff}} = N_A/N_B$), defined by the ratio of N_A to implanted B concentration (N_B) evaluated by SIMS, was estimated to be 36%, which is about four times higher than the previously reported efficiency for heavily B-doped diamond with almost the same density.[16,17] In the case of the RT implantation shown in Fig. 6, the estimated acceptor and donor concentrations were respectively 2.8×10^{19} and $4.7 \times 10^{18}\,\mathrm{cm}^{-3}$, suggesting that the D_{eff} was greatly enhanced to 78%, which is 8.7 and 5.2 times higher than the previous results for similar doping concentration reported by Tsubouchi et al. and Vogel et al., respectively. Both acceptor and donor concentrations slightly decreased to $1.7 \times 10^{19}\,\mathrm{cm}^{-3}$ and $2.9 \times 10^{18}\,\mathrm{cm}^{-3}$, respectively, and the doping efficiency was eventually estimated to be ~50% for the 1300 °C-postannealed sample. The electrical parameters obtained by Hall effect measurement are summarized in Table I. Based on the fact that the compensation ratio for the RT-implanted sample did not significantly change, higher-temperature annealing decreases both substitutional B atoms and donor-like center concentrations. The reasons the electrical properties were significantly improved are not yet evident through the present experiments; however, the quality improvement of diamond substrates during several decades is thought to be one of the reasons for obtaining excellent electrical properties. The decrement of numbers of intrinsically incorporated impurities and introduced primary defects such as vacancies and interstitials formed during synthesis processes is also supposed to decrease secondary defect formation such as dislocations, stacking faults or defect complexes during implantation and postannealing processes. Defect-free diamond substrates therefore undoubtedly decrease the diffusion of defects and impurities during implantation and postannealing, resulting in the lower processing temperature and eventually the excellent electrical properties.[31–33] We would like to emphasize that in Si device fabrication processes, the optimum processing temperature decreases with the great improvement of substrate quality of crystalline Si wafer.

Figure 7 shows specific resistance (σ^{-1}) for the 900 °C-implanted (a) and RT-implanted (b) samples followed by 1150 °C (black), 1300 °C (red) and 1450 °C (green) annealing. The solid curves show the theoretically calculated resistivity in accordance with the following formalism. The dashed line ($E_A = 0.1$ eV) in the figure is guide for the eye. The temperature-dependent resistivity was found to be significantly changed around RT (~300 K): there are two activation energies at higher (>RT) and lower (<RT) temperature regions. This suggests that the hopping conduction has been dominant below RT. The temperature at which the electrical conduction mechanism changes from band to hopping largely depends on the postannealing temperature.

3.2. Dominant conduction mechanisms

Next, we quantitatively introduce the analytical procedure of specific resistance shown with solid curves in Fig. 7. Figure 8 schematically shows the impurity band diagram of B acceptor levels for B-doped diamond in accordance with the following relations as a function of N_A. The electric conductivity σ for impurity-doped semiconductors is generally described by three conductive elements of σ_1, σ_2 and σ_3. The substantial conductivity σ can be expressed by the summation of these components.

$$\sigma = \sigma_1 + \sigma_2 + \sigma_3, \tag{4}$$

$$\sigma_1 = ep\mu, \tag{5}$$

$$\sigma_2 = \sigma_{02} \cdot \exp\left(-\frac{\epsilon_2}{k_B T}\right), \tag{6}$$

$$\sigma_3 = \sigma_{03}^{\mathrm{NNH}} \cdot \exp\left(-\frac{\epsilon_3}{k_B T}\right) + \sigma_{03}^{\mathrm{VRH}} \cdot \exp\left(-\frac{T_0}{T}\right)^n. \tag{7}$$

In the case of p-type semiconductors, the σ_1 conduction is derived from the ionization of holes from the neutral acceptor level to the valence band. The activation energy corresponds to the ionization energy of a single isolated acceptor. For relatively heavily doped semiconductors, the impurity levels are significantly broadened due to the overlap of acceptor wave functions, resulting in the formation of narrow impurity bands. The impurity band widths of ground and excited states thus depend on the doped impurity concentration. The σ_2 conduction is derived from holes excited from the neutral impurity band (A^0) to the positively charged band (A^+), as shown in Fig. 8, and appears under specific conditions with low compensation ratio ($K < 0.2$) at high impurity

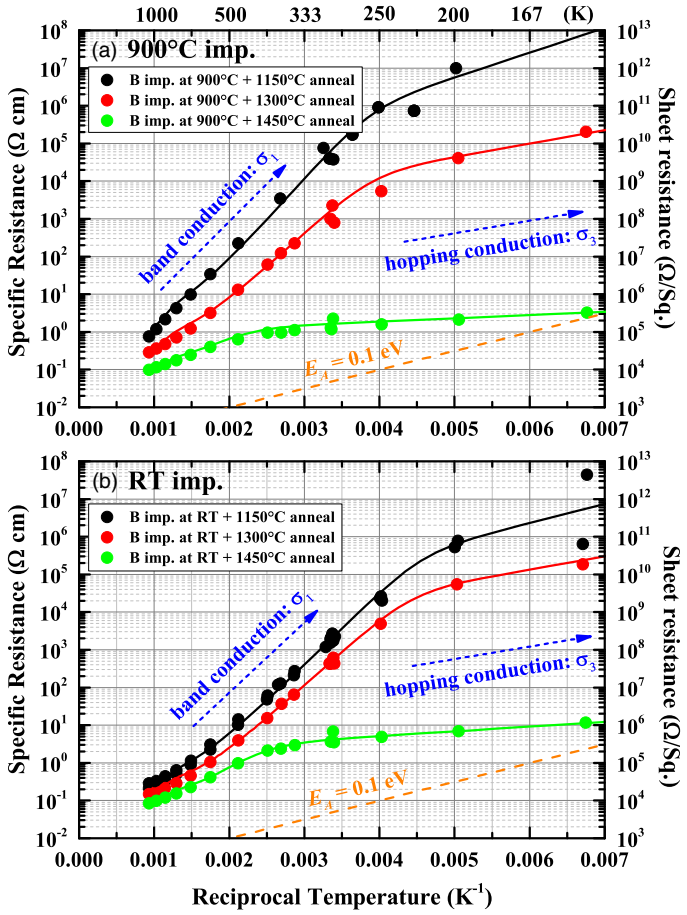

Fig. 7. (Color online) Sheet and specific resistance for the B-implanted samples at 900 °C and RT followed by 1150 °C (black dots), 1300 °C (red dots) and 1450 °C (green dots) annealing. Solid curves show the theoretical results based on the inverse of Eq. (4). The dashed line ($E_A = 0.1$ eV) in the figure is guide for the eye.

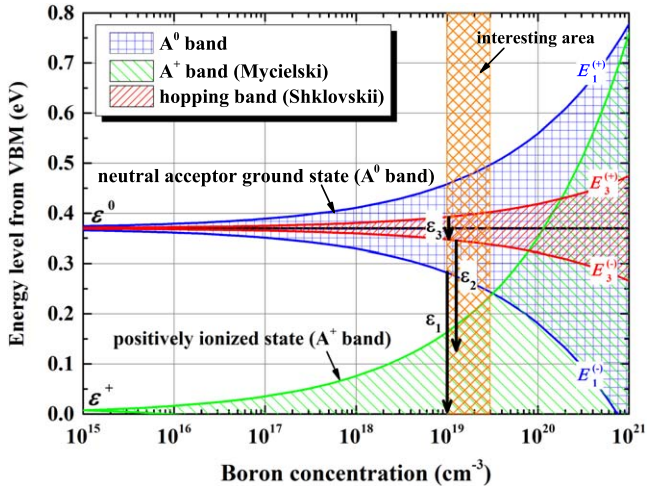

Fig. 8. (Color online) Impurity band diagram of B acceptor levels doped into diamond as a function of N_A.

concentration near Mott transition. The σ_3 conduction is known as the intraband hopping process, derived from hopping theory, which will be discussed later [Eq. (17)].[34] The first and second terms in Eq. (7) are related to the nearest neighbor hopping (NNH) and variable range hopping (VRH), respectively. Here, T_o and n are the specific parameters of VRH conduction, which can be referred in the previous reports.[34–36] With decreasing temperatures, σ_1 or σ_2 conductions are changed to the NNH regime [$\propto \exp(-\epsilon_3/k_B T)$], where ϵ_3 corresponds to the energy barrier between neighboring energy states.[37] At enough low temperatures, the NNH regime is eventually altered to the VRH [$\propto \exp(-(T_0/T)^n$].[38]

It is well known that the highest and lowest energy level of neutral B acceptor band ($E_1^{(\pm)}$) with respect to valence band maximum can be written as,[34,39]

$$E_1^{(\pm)} = \mathcal{E}^0 \pm \gamma \frac{e^2}{\kappa R}. \tag{8}$$

Here, the $\mathcal{E}^0$ and κ indicate the ionization energy of a single isolated acceptor and dielectric constant of diamond, known to be $\mathcal{E}^0 = 0.37$ eV for acceptor B and $\kappa = 5.7$, respectively. R is defined as the nearest neighbor distance of acceptors, $(3/4\pi N_A)^{1/3}$ and γ is around unity.[40] In this case of $N_A = 10^{19}\,\mathrm{cm}^{-3}$, ϵ_1, corresponding to $E_1^{(-)}$, is to be $\sim$0.3 eV. The A^0 band width Ω_1 is thus written as,

$$\Omega_1 = \frac{2e^2}{\kappa}\left(\frac{3}{4\pi N_A}\right)^{-\frac{1}{3}}. \tag{9}$$

According to Mycielski et al., the energy level of ϵ_2, which is not clearly defined, is simply described to be,[39,41]

$$\epsilon_2 \approx \mathcal{E}^0 - 3\left(\frac{e^2}{\kappa}\right)N_A^{1/3}. \tag{10}$$

In the case of $N_A = 10^{19}\,\mathrm{cm}^{-3}$, ϵ_2 can be estimated to be $\sim$0.20 eV. More recently, Baskin et al. proposed the σ_2

conduction mechanism based on delocalized A^0 and A^+ bands:[42]

$$\epsilon_2 = (\mathcal{E}^0 - \mathcal{E}^+) - \mathcal{E}_c - \frac{\epsilon_3}{2}. \quad (11)$$

Here, $\mathcal{E}^+$ and $\mathcal{E}_c$ are the energy levels of the excited state (A^+) and the mobility edge in the A^+ band, respectively. The mobility edge can be estimated from the overlap integral of acceptor wave functions. The meaningful excitation contributing to electrical conduction is holes excited above $\mathcal{E}_c$; consequently, ϵ_2 is smaller than the average energy gap ($U = \mathcal{E}^0 - \mathcal{E}^+$) between A^0 and A^+ bands.[43]

Shklovskii et al. proposed the activation energy ϵ_3 as,

$$\epsilon_3 = 0.99\left(\frac{e^2}{\kappa}\right)N_A^{1/3}(1 - 0.3K^{1/4}), \quad (12)$$

$$\sim 0.054 \text{ eV} \left(\text{for } N_A = 10^{19} \text{ cm}^{-3}, 1 - \frac{1}{K} \ll 0\right), \quad (13)$$

$$E_3^{(\pm)} = \mathcal{E}^0 \pm \frac{\epsilon_3}{2}, \quad (14)$$

for low compensation limit.[44,45] The band width (Ω_3) involving the σ_3 conduction will be,

$$\Omega_3 \geqslant \epsilon_3. \quad (15)$$

The energy width (Ω_3) of σ_3 conduction should be smaller than that of Ω_1; typically one third of Ω_1.

As shown in Fig. 7, the observed activation energy below RT was less than 0.1 eV, indicating that the electrical conduction below RT was probably governed by σ_3 hopping conduction. According to Massarani et al.,[34] the transition probability (P) of hole hopping from an occupied site to an unoccupied site can be expressed as the following relation:

$$P = \nu_{ph} \cdot \exp\left(-2\alpha R - \frac{w}{k_B T}\right), \quad (16)$$

where $\nu_{ph} = 4 \times 10^{13}$ Hz corresponds to the maximum phonon frequency, R is a distance between neighboring hopping sites defined as $(3/4\pi N_A)^{1/3}$, and α^{-1} is a localization length of an acceptor wave function; to be $\sqrt{2m^*\mathcal{E}^0}/\hbar$. w is the energy difference between neighboring hopping sites, corresponding to ϵ_3. If $2\alpha R$ is relatively larger than w/k_BT, the conduction is preferably governed by the hopping process between the nearest neighbor sites. On the other hand, hopping to a far site with small energy difference will preferentially take place in the case of $2\alpha R < w/k_BT$ (VRH). Under the present condition, $2\alpha R$ is relatively larger than w/k_BT near RT, even if we assume the maximum value of $w \sim \Omega_3$. It is indicated that the dominant contribution of hole transport is mainly attributed to the NNH regime. This is consistent with the previous reports.[28,46] In accordance with Einstein's relation, hopping conductivity σ_3 is finally expressed as,

$$\sigma_3 = \frac{3e^2}{4\pi f}\frac{\nu_{ph}}{wR} \cdot \exp\left(-2\alpha R - \frac{w}{k_B T}\right), \quad (17)$$

where f is a coordination number of acceptors in diamond lattice, typically adopted as 6 in the previous reports.[33,34]

We eventually fit the experimentally obtained specific resistance shown in Fig. 7 by the theoretical relations (σ^{-1}) using Eqs. (5) and (17) with only two fitting parameters of the localization length α^{-1} and activation energy w. Here, the parameters of μ and p in Eq. (5) were referred from experimentally determined values by Hall effect measurements discussed in Figs. 2 and 3. The best-fit curves and obtained parameters are shown in Fig. 7 and Table II for the 1300 °C- and 1450 °C-postannealed samples. The activation energy ϵ_3 and localization length for 1300 °C-annealed samples were estimated to be 0.070 eV and 5–6 $\times 10^{-8}$ cm, respectively. The observed ϵ_3 corresponds to the theoretically predicted value for NNH conduction [Eq. (13)], and the obtained α^{-1} took the value close to the effective Bohr radius, but was somewhat larger. After 1450 °C annealing, the resistivity and activation energy were significantly decreased. The localization length was increased to be at least 8.5×10^{-8} and 9.0×10^{-8} cm for each sample; however, the value could not be uniquely determined, due to the lack of accurate N_A in the Hall measurements. The increase of the localization length in the higher-temperature annealing stage clearly shows the enhancement of the overlap of impurity wave functions. This increment of the localization length induces connection of the percolation channels of conduction in the impurity bands, resulting in the appearance of hopping conduction. It is because extremely high-temperature annealing promotes the diffusion and recombination of created defects, which causes the formation of new products such as graphite-like or disordered microstructures.[31–33]

Table II. Obtained parameters for hopping conduction.

Temperature (implant.)	Temperature (postanneal)	Activation energy ϵ_3 (eV)	Localization length α^{-1} (cm)
RT	1300 °C	0.070	5.0×10^{-8}
	1450 °C	0.025	$>8.5 \times 10^{-8}$
900 °C	1300 °C	0.070	5.7×10^{-8}
	1450 °C	0.015	$>9.0 \times 10^{-8}$

Consequently, effective B doping should be performed by low-temperature implantation at around RT followed by annealing at relatively low temperatures from 1150 °C–1300 °C. Effective B doping is probably related to the diffusion and recombination of created defects during ion implantation and postannealing.[47–50]

4. Conclusions

The electrical properties of heavily B-doped diamond formed by ion implantation were comprehensively investigated from the viewpoints of temperatures in B^+ ion implantation and postannealing. We compared the electrical properties for shallowly and flatly B^+ ion-implanted type IIa diamond substrates at 900 °C and RT, with a flat concentration of 3.5×10^{19} cm^{-3}. These samples were subsequently annealed at 1150 °C, 1300 °C and 1450 °C after ion implantation. The electrical properties of the compensation ratio and doping efficiency for the 900 °C-implanted samples were not sufficiently improved even by high-temperature annealing. On the other hand, the B implantation at RT followed by postannealing at 1150 °C and 1300 °C realized the excellent properties of doping efficiency (78%), Hall mobility (108 cm^{2}V^{-1}s^{-1}) and resistivity for the RT-implanted sample. We confirmed p-type conductivity and typical ionization energy of acceptor B atoms at a wide temperature

range from 173–1073 K for both samples. The accomplishment of effective B doping at lower-temperature processes is probably realized by the decrement of intrinsically incorporated defects in substrates when they are synthesized. This decrement of primary defects effectively reduced new defect creations during the ion implantation and postannealing stages.

Acknowledgments

We gratefully acknowledge Prof. Mizuno and Mr. Saito for their support in setting up the experiments and for their various suggestions. This study was partly supported by grant-aid from the Research Institute for Integrated Science, Kanagawa University (Grant No. RIIS201702).

1) C. E. Nebel and J. Ristein, *Semiconductors and Semimetals* (Elsevier, Amsterdam, 2003) 76.
2) A. Paoletti and A. Tucciarone, *Proceedings of the International School of Physics "Enrico Fermi"* (IOS Press, Bologna, 1997) 135, The Physics of Diamond.
3) L. Pan and E. Kania, *Diamond: Electrical Properties and Applications* (Kluwer, Boston, MA, 1995).
4) J.-P. Lagrange, A. Deneuville, and E. Gheeraert, Carbon **37**, 807 (1999).
5) R. F. Mamin and T. Inushima, Phys. Rev. B **63**, 033201 (2001).
6) J. Pernot, P. N. Volpe, F. Omnés, P. Muret, V. Mortet, K. Haenen, and T. Teraji, Phys. Rev. B **63**, 033201 (2010).
7) M. Aono, O. Maida, and T. Ito, Diamond Relat. Mater. **20**, 1357 (2011).
8) J. F. Prins, Phys. Rev. B **38**, 5576 (1988).
9) J. F. Prins, Appl. Phys. Lett. **76**, 2095 (2000).
10) J. F. Prins, Diamond Relat. Mater. **11**, 612 (2002).
11) J. F. Prins, Semicond. Sci. Technol. **18**, S27 (2003).
12) C. Uzan-Saguy, R. Kalish, R. Walker, D. N. Jamieson, and S. Prawer, Diamond Relat. Mater. **7**, 1429 (1998).
13) T. Vogel, J. Meijer, and A. Zaitsev, Diamond Relat. Mater. **13**, 1822 (2004).
14) F. Fontaine, C. Uzan-Saguy, B. Philosoph, and R. Kalish, Appl. Phys. Lett. **68**, 2264 (1996).
15) N. Tsubouchi, M. Ogura, Y. Horino, and H. Okushi, Appl. Phys. Lett. **89**, 012101 (2006).
16) N. Tsubouchi and M. Ogura, Jpn. J. Appl. Phys. **47**, 7047 (2008).
17) N. Tsubouchi, M. Ogura, N. Mizuochi, and H. Watanabe, Diamond Relat. Mater. **18**, 128 (2009).
18) K. Ueda and M. Kasu, Diamond Relat. Mater. **17**, 502 (2008).
19) Y. Seki, Y. Hoshino, and J. Nakata, Appl. Phys. Lett. **115**, 072103 (2019).
20) J. F. Ziegler, J. P. Biersack, and U. Littmark, *The Stopping and Range of Ions in Solids* (Pergamon, Oxford, 1985).
21) A. T. Collins and A. W. S. Williams, J. Phys. C **4**, 1789 (1971).
22) F. Fontaine, J. Appl. Phys. **85**, 1409 (1999).
23) P.-N. Volpe, J. Pernot, P. Muret, and F. Omnés, Appl. Phys. Lett. **94**, 092102 (2009).
24) M. Gabrysch, S. Majdi, A. Hallén, M. Linnarsson, A. Schöner, D. Twitchen, and J. Isberg, Phys. Stat. Sol. (a) **205**, 2190 (2008).
25) K. Tsukioka and H. Okushi, Jpn. J. Appl. Phys. **45**, 8571 (2006).
26) V. Mortet, M. Daenen, T. Teraji, A. Lazea, V. Vorlicek, J. D'Haen, K. Haenen, and M. D'Olieslaeger, Diamond Relat. Mater. **17**, 1330 (2008).
27) T. Teraji, H. Wada, M. Yamamoto, K. Arima, and T. Ito, Diamond Relat. Mater. **15**, 602 (2006).
28) M. Werner, R. Locher, W. Kohly, D. S. Holmes, S. Klose, and H. J. Fecht, Diamond Relat. Mater. **6**, 308 (1997).
29) M. Werner, R. Job, A. Zaitzev, W. R. Fahrner, W. Seifert, C. Johnston, and P. R. Chalker, Phys. Stat. Sol. (a) **154**, 385 (1996).
30) T. H. Borst and O. Weis, Phys. Stat. Sol. (a) **154**, 423 (1996).
31) S. Ogawa, T. Yamada, S. Ishizduka, A. Yoshigoe, M. Hasegawa, Y. Teraoka, and Y. Takakuwa, Jpn. J. Appl. Phys. **51**, 11PF02 (2012).
32) N. Tokuda, M. Fukui, T. Makino, D. Takeuchi, S. Yamasaki, and T. Inokuma, Jpn. J. Appl. Phys. **52**, 110121 (2013).
33) T. Matsumoto, H. Kato, N. Tokuda, Y. Makino, M. Ogura, D. Takeuchi, H. Okushi, and S. Yamasaki, Phys. Status Solidi **8**, 137 (2014).
34) B. Massarani, J. C. Bourgoin, and R. M. Chrenko, Phys. Rev. B **17**, 1758 (1978).
35) N. F. Mott and E. A. Davies, *Electronic Processes in Non-Crystalline Materials* (Clarendon, Oxford, 1971).
36) A. L. Efros and B. I. Shklovskii, J. Phys. C **8**, L49 (1975).
37) B. I. Shklovskii and A. L. Efros, *Electronic Properties of Doped Semiconductors* (Springer, Berlin, 1984).
38) H. Liu, A. Pourret, and P. Guyot-Sionnest, ACS Nano **4**, 5211 (2010).
39) J. Mycielski, Phys. Rev. **123**, 99 (1961).
40) G. L. Peason and J. Bardeen, Phys. Rev. **75**, 865 (1949).
41) F. H. Pollak, Phys. Rev. **138**, A618 (1965).
42) E. Baskin, A. Reznik, D. Saada, J. Adler, and R. Kalish, Phys. Rev. B **64**, 224110 (2001).
43) E. Gheeraert, S. Koizumi, T. Teraji, H. Kanda, and M. Nesládek, Phys. Status Solidi (a) **174**, 39 (1999).
44) B. I. Shklovskii, A. L. Efros, and I. Y. Yanehef, JETP Lett. **14**, 233 (1971).
45) B. I. Shklovskii, A. L. Efros, and I. Y. Yanehef, Phys. Status Solidi (b) **50**, 45 (1972).
46) J.-P. Lagrange, A. Deneuville, and E. Gheeraeri, Diamond Relat. Mater. **7**, 1390 (1998).
47) G. Davies, S. C. Lawson, A. T. Collins, A. Mainwood, and S. J. Sharp, Phys. Rev. B **46**, 13157 (1992).
48) A. Allers, A. T. Collins, and J. Hiscock, Diamond Relat. Mater. **7**, 228 (1998).
49) J. Bernholc, A. Antonelli, T. M. Del Sole, Y. Bar-Yam, and S. T. Pantelides, Phys. Rev. Lett. **61**, 2689 (1988).
50) A. Mainwood, F. P. Larkins, and A. M. Stoneham, Solid-state Electron **21**, 1431 (1978).

